

On-Demand Directional Photon Emission using Waveguide Quantum Electrodynamics

Bharath Kannan,^{1, 2, *, †} Aziza Almanakly,^{1, 2, *} Youngkyu Sung,^{1, 2} Agustin Di Paolo,¹ David A. Rower,^{1, 3} Jochen Braumüller,¹ Alexander Melville,⁴ Bethany M. Niedzielski,⁴ Amir Karamlou,^{1, 2} Kyle Serniak,⁴ Antti Vepsäläinen,¹ Mollie E. Schwartz,⁴ Jonilyn L. Yoder,⁴ Roni Winik,¹ Joel I-Jan Wang,¹ Terry P. Orlando,^{1, 2} Simon Gustavsson,¹ Jeffrey A. Grover,¹ and William D. Oliver^{1, 2, 3, 4}

¹Research Laboratory of Electronics, Massachusetts Institute of Technology, Cambridge, MA 02139, USA

²Department of Electrical Engineering and Computer Science,

Massachusetts Institute of Technology, Cambridge, MA 02139, USA

³Department of Physics, Massachusetts Institute of Technology, Cambridge, MA 02139, USA

⁴MIT Lincoln Laboratory, Lexington, MA 02421, USA

Routing quantum information between non-local computational nodes is a foundation for extensible networks of quantum processors. Quantum information can be transferred between arbitrary nodes by photons that propagate between them, or by resonantly coupling nearby nodes. Notably, conventional approaches involving propagating photons have limited fidelity due to photon loss and are often unidirectional, whereas architectures that use direct resonant coupling are bidirectional in principle, but can generally accommodate only a few local nodes. Here, we demonstrate high-fidelity, on-demand, bidirectional photon emission using an artificial molecule comprising two superconducting qubits strongly coupled to a waveguide. Quantum interference between the photon emission pathways from the molecule generate single photons that selectively propagate in a chosen direction. This architecture is capable of both photon emission and capture, and can be tiled in series to form an extensible network of quantum processors with all-to-all connectivity.

I. INTRODUCTION

Most realistic architectures of large-scale quantum computing employ quantum networks: the high-fidelity communication of quantum information between distinct non-local processing nodes [1]. Quantum networking enables modular and extensible quantum computation by distributing entanglement between computational nodes [2]. There are several possible methods for realizing quantum networking, including the routing of optical photons between trapped-ion modules [3], coupling emitters to photonic waveguides [4, 5] or optical nanofibers [6–9], shuttling ions [10, 11] or neutral atoms [12] between qubit arrays, or cavity-assisted pairwise coupling between natural or solid-state artificial atoms [13–18]. Enabling non-local quantum communication is particularly relevant for qubits which are natively limited to nearest-neighbour coupling, such as 2D arrays of surface-trapped ions, semiconducting qubits, and superconducting qubits.

Experimental realizations of communication between superconducting qubits have typically relied on coherent coupling via resonators [13–17] or itinerant photons that propagate in unidirectional waveguides [19–21]. While the former approach has achieved the highest fidelities to date, it is not easily extensible. For example, the free spectral range of the coupling resonator constrains the maximal distance between the nodes. Alternatively, itinerant photons that propagate along waveguides do not have this limitation. However, the fi-

dentity of this approach has been limited as lossy non-reciprocal components, such as circulators, are required to prevent undesirable standing waves between nodes and render waveguides—that are naturally bidirectional—unidirectional. Instead, an architecture that uses conventional bidirectional waveguides, but with the ability to generate photons which propagate in a chosen direction, would enable both high-fidelity and high-connectivity communication within a quantum network.

Recent theoretical work has shown that superconducting circuits in a waveguide quantum electrodynamics (QED) architecture are capable of realizing such a network [22]. In waveguide QED, atoms are directly coupled to the continuum of propagating photonic modes in a waveguide [23]. Realizing the strong coupling regime of waveguide QED has enabled a wide range of phenomena to be experimentally observed, such as resonance fluorescence [24–27], Dicke super- and sub-radiance [28–30], and giant artificial atoms [31–35]. Importantly, the achievable strong coupling between superconducting qubits and itinerant photons also allows the qubits to be used as high-quality quantum emitters [36–43].

In this work, we experimentally demonstrate on-demand directional photon emission based on the quantum interference of indistinguishable photons emitted by a giant artificial molecule. We arrange qubits that are spatially separated along a bidirectional waveguide to form a giant artificial molecule that can both emit and absorb photons in a chosen direction [22]. We use quadrature amplitude detection to obtain the moments of the two output fields of the waveguide. Using these moments, we reconstruct the state of the generated photon and quantify its fidelity. The architecture realized here can be used to form the basis of a quantum network that is capable of non-local and all-to-all connectivity.

* These authors contributed equally.

† bkannan@mit.edu

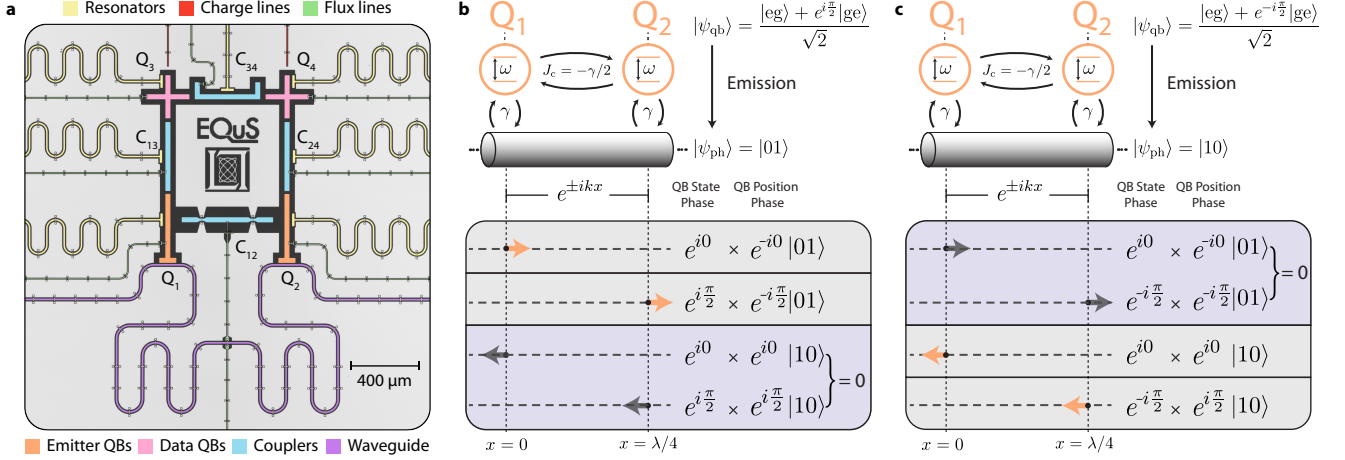


FIG. 1. Directional emission in a waveguide QED architecture. **a)** A false-colored optical micrograph of the device. The state of the data qubits (pink) is transferred into the emitter qubits (orange) via an exchange interaction mediated by tunable couplers (blue). The emitter qubits continuously emit any population into the waveguide (purple). **b)** Schematic diagram of the two resonant emitter qubits Q_1 and Q_2 coupled to a common waveguide with equal strength γ and separated by a distance $\lambda/4$. The phase delay for photons in the waveguide is given by $e^{\pm ikx}$, where $k = 2\pi/\lambda$ is the photon wavevector and λ is the photon wavelength. The sign of this phase delay is determined by the propagation direction of the photon (+ for leftward, and - for rightward). An external coupler-mediated exchange interaction of strength $J_c = -\gamma/2$ is applied in order to fully cancel the waveguide mediated interaction between the qubits. The four possible coherent pathways for a photon to be emitted by the qubits into the left/right travelling modes of the waveguide are shown below. Each pathway obtains a phase from the initial state $|\psi_{qb}\rangle$ and position x of the qubit that is emitting a photon. When the qubits are initialized into $|\psi_{qb}\rangle = (|eg\rangle + e^{i\pi/2}|ge\rangle)/\sqrt{2}$, the emitted photon only propagates towards the right due to destructive interference between the left-propagating pathways. **c)** The same setup as (b), but with the initial qubit state $|\psi_{qb}\rangle = (|eg\rangle + e^{-i\pi/2}|ge\rangle)/\sqrt{2}$. In this case, the right-propagating pathways destructively interfere, and the emitted photon only propagates towards the left.

II. EXPERIMENT

Our device comprises of four frequency-tunable transmon qubits [44] and four tunable transmon couplers [45, 46] between each neighboring qubit pair, as shown in Fig. 1a. The artificial molecule comprises two qubits Q_1 and Q_2 , each of which resonantly emits photons with a frequency of $\omega_1/2\pi = \omega_2/2\pi = 4.93$ GHz, are equally coupled to a common waveguide with strength $\gamma/2\pi = 3.2$ MHz, and are spatially separated along the waveguide by a distance $\Delta x = \lambda/4$, where λ is the wavelength of the emitted photon. The remaining two qubits, Q_3 and Q_4 , serve as data qubits that are not subject to direct dissipation into the waveguide. These qubits would act as the interface between a quantum processor and the emitter qubits within a node. The state of Q_3 and Q_4 can be prepared with high fidelity with a combination of single- and two-qubit gates. Photons are generated by transferring the state of the data qubits $Q_{3/4}$ to the emitter qubits $Q_{1/2}$ via an exchange interaction mediated by the couplers $C_{13/24}$.

A. Protocol for Directional Emission

The physics of the directional emission protocol is determined by the dynamics of the sub-system compris-

ing the emitter qubits $Q_{1/2}$ and the waveguide. For $\Delta x = \lambda/4$, the master equation that determines the time evolution of the emitters is [22, 23]:

$$\partial_t \hat{\rho} = -i[\hat{H}_{qb} + \hat{H}_c, \hat{\rho}] + \gamma \sum_j^2 D[\hat{\sigma}_j^-] \hat{\rho}, \quad (1)$$

where $\hat{\rho}$ is the density matrix of the sub-system, $D[\hat{O}] = \hat{O}\hat{\rho}\hat{O}^\dagger - \frac{1}{2}\{\hat{O}^\dagger\hat{O}, \hat{\rho}\}$ is the Lindblad dissipator, $\hat{H}_{qb} = \sum_j \omega_j \hat{\sigma}_j^+ \hat{\sigma}_j^-$ is the bare Hamiltonian of the emitter qubits, and $\hat{\sigma}_j^\pm$ are the raising and lowering Pauli operators with $j \in \{1, 2\}$. Finally, $\hat{H}_c = (\gamma/2 + J_c)(\hat{\sigma}_1^+ \hat{\sigma}_2^- + \hat{\sigma}_2^+ \hat{\sigma}_1^-)$ accounts for the exchange coupling between the qubits from two sources: a static waveguide-mediated interaction with strength $\gamma/2$ and a tunable-coupler-mediated interaction (via C_{12}) with strength J_c . The tunability in J_c is used to cancel the waveguide-mediated interaction such that the emitters are decoupled from each other.

The final state of the photons emitted by Q_1 and Q_2 depends on the interference between their simultaneous emission. Specifically, when the initial state of the emitter qubits is

$$|\psi^\pm\rangle = \frac{|eg\rangle + e^{\pm i\pi/2}|ge\rangle}{\sqrt{2}}, \quad (2)$$

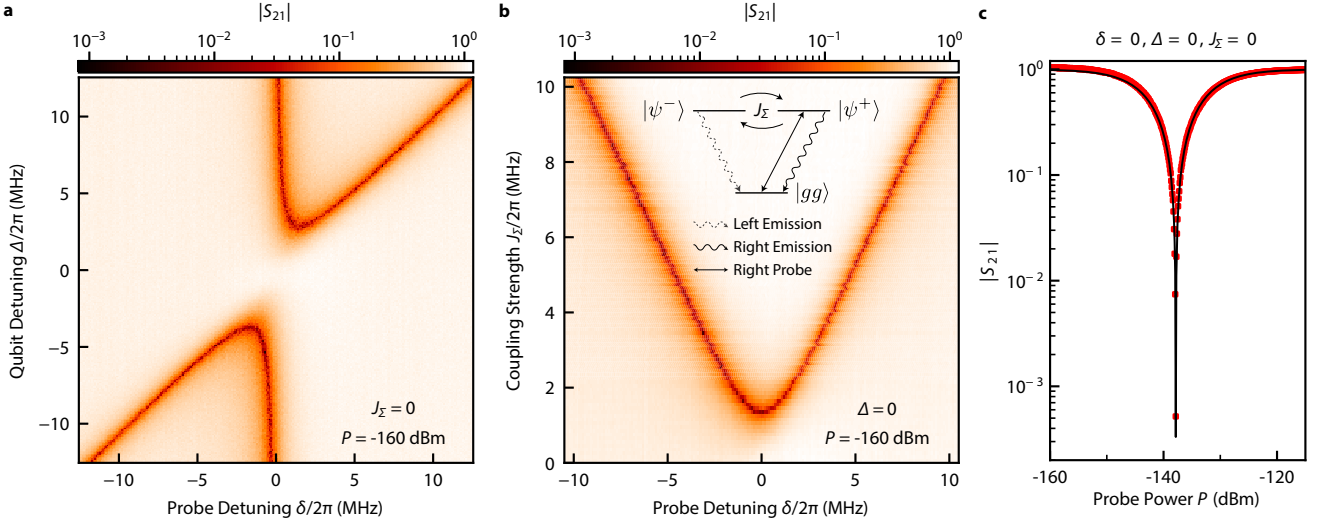


FIG. 2. Verifying protocol conditions via elastic scattering. **a)** The transmittance $|S_{21}|$ of an input probe tone incident upon the two emitter qubits Q_1 and Q_2 through the waveguide. $|S_{21}|$ is plotted as a function Δ , the detuning of Q_2 from Q_1 , and δ , the detuning between the probe and Q_1 . When the qubits are far from resonance with each other ($\Delta > \gamma$), they will act as mirrors ($|S_{21}| \ll 1$) to the probe if the probe is resonant with either qubit ($\delta = 0, \Delta$). However, when the qubits are resonant ($\Delta = 0$), the transmittance returns to unity. **b)** $|S_{21}|$ as a function of the total coupling strength $|J_\Sigma|$ and δ while keeping Q_1 and Q_2 resonant and using the same probe power as in (a). The level diagram of the three states $|gg\rangle$, $|\psi^+\rangle$, and $|\psi^-\rangle$ is shown as an inset ($|ee\rangle$ is ignored for weak probes). The rightward-propagating probe used to obtain this data only couples the states $|gg\rangle \leftrightarrow |\psi^+\rangle$, and a finite exchange interaction between the emitters will couple $|\psi^+\rangle \leftrightarrow |\psi^-\rangle$. The state $|\psi^+\rangle$ can only emit a rightward-propagating photon and $|\psi^-\rangle$ can only emit a leftward-propagating photon. We observe two dips in the transmission at $\delta = \pm J_\Sigma$, corresponding to the energy splitting from the hybridization of $|\psi^\pm\rangle$. When $|J_\Sigma| \rightarrow 0$, the transmission approaches unity for all δ because $|\psi^+\rangle$ is the only state that is excited, and it can only emit in the same direction (right) as the probe. This measurement is used to set $|J_\Sigma| = 0$. **c)** The measured $|S_{21}|$ (red points) as a function of the probe power with $\Delta = 0$, $\delta = 0$, and $J_\Sigma = 0$. The data agrees well with a fit (black curve) to a master equation simulation.

the node will emit a single photon that propagates either leftward or rightward, depending on the sign of the relative phase. To see this, consider the emitter qubits initialized to $|\psi_{qb}\rangle = |\psi^+\rangle$, as shown in Fig. 1b. There are four emission pathways from this state, each involving one of the emitter qubits, Q_1 or Q_2 , releasing a photon that propagates towards the left or the right. For simplicity, we define the positions of Q_1 and Q_2 along the waveguide to be $x = 0$ and $x = \Delta x$, respectively. The pathways with a photon emitted by Q_2 will accumulate additional phases from both the relative phase $e^{i\pi/2}$ in $|\psi^+\rangle$ and a phase $e^{\pm ik\Delta x}$ from the position of Q_2 relative to Q_1 . Here, $k = 2\pi/\lambda$ is the wavevector of the emitted photon, and the sign of the phase is determined by the propagation direction of the photon (+ for leftward, and - for rightward). These additional phases result in the total constructive (destructive) interference between the pathways that involve a photon propagating towards the right (left). Therefore, the emitted photon solely propagates to the right in the state $|\psi_{ph}\rangle = |01\rangle$, where $|n_L n_R\rangle$ denotes the number of photons in the leftward- and rightward-propagating modes of the waveguide. A similar analysis for the initial qubit state $|\psi_{qb}\rangle = |\psi^-\rangle$ is shown in Fig. 1c, indicating that the emitted photon propagates towards the left in the state $|\psi_{ph}\rangle = |10\rangle$ in

this case.

The directional emission can be formally verified using the input-output relations for leftward- and rightward-propagating modes in the waveguide: [23]

$$\begin{aligned} \hat{a}_L &= \hat{a}_L^{\text{in}} + \sqrt{\frac{\gamma}{2}}(\hat{\sigma}_1^- + \hat{\sigma}_2^- e^{ik\Delta x}), \\ \hat{a}_R &= \hat{a}_R^{\text{in}} + \sqrt{\frac{\gamma}{2}}(\hat{\sigma}_1^- + \hat{\sigma}_2^- e^{-ik\Delta x}). \end{aligned} \quad (3)$$

Here, $\hat{a}_{L(R)}^{\text{in}}$ represents the input field of photons in the waveguide for the leftward (rightward) propagating mode. From these relations, the number of photons in either mode of the waveguide, $\langle \hat{N}_{L(R)} \rangle = \langle \hat{a}_{L(R)}^\dagger \hat{a}_{L(R)} \rangle$, can be directly related to the state of the qubits. Given that the emitters are initialized into one of $|\psi^\pm\rangle$, the interference described above is only perfect when $\Delta x = (2n+1)\lambda/4$, where n is an integer, and $J_c = -\gamma/2$. The first condition ensures that the interfering emission pathways are fully in/out of phase. Additionally, it is the only spatial separation for which there is no correlated dissipation between the qubits [23], which would further disturb the interference. The second condition prevents any population transfer between the qubits during the emission process by setting the exchange Hamiltonian \hat{H}_c to zero.

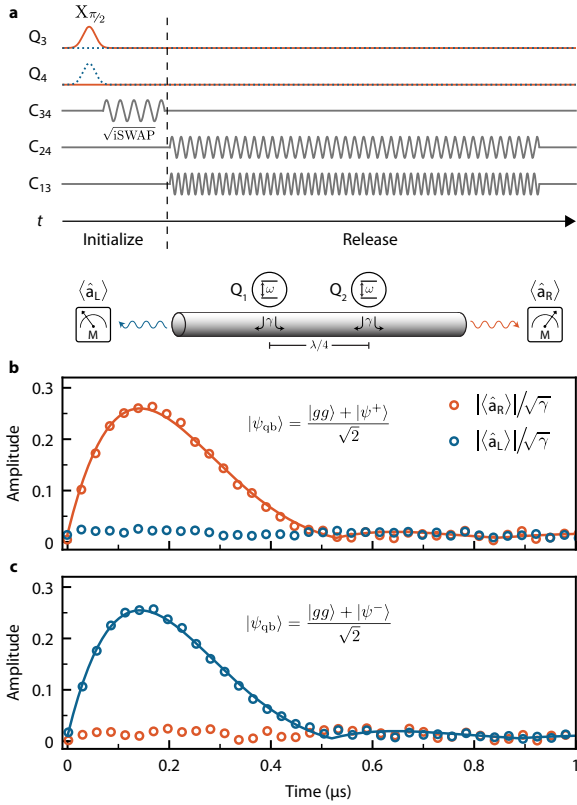


FIG. 3. Pulse sequence and time-domain measurements. **a)** The pulse sequence for generating a photon. The qubit state initialization begins by exciting either Q_3 (orange solid curve) or Q_4 (blue dashed curve). These qubits are then entangled via a \sqrt{i} SWAP gate by parametrically modulating the frequency of the tunable coupler C_{34} at the detuning of Q_3 and Q_4 . Finally, a photon is released via a parametric exchange interaction between the data qubits $Q_{3/4}$ and the emitter qubits $Q_{1/2}$. The measurement schematic below the pulse-sequence shows that the field amplitudes $\hat{a}_{L/R}$ are acquired at both outputs of the waveguide. **b)** The measured (circles) time-dependent field amplitudes for a photon emitted towards the right. The data is fit (solid curve) using the solution to the master equation (see Supplementary Info.). The initial state of the data qubits is $|\psi_{qb}\rangle = (|gg\rangle + |\psi^+\rangle)/\sqrt{2}$. The field amplitude of the leftward emission channel is nearly zero. **c)** The same measurement as (b), but with $|\psi_{qb}\rangle = (|gg\rangle + |\psi^-\rangle)/\sqrt{2}$ such that the emitted photon now propagates to the left.

B. Device Calibration for Directional Emission

Verifying that the ideal directional emission conditions are satisfied in the experiment is challenging. In particular, the strong and always-on dissipation into the waveguide makes it difficult to measure the strength of the coupling between the emitters, $J_\Sigma = \gamma/2 + J_c$. The typical methods, such as observations of avoided crossings in qubit spectroscopy or population exchange in time domain, are limited in resolution when outside the strong coupling regime where $J_\Sigma < \gamma$. To go beyond this limit, we infer the value of J_Σ by measuring the elastic scatter-

ing of a weak input probe tone. Specifically, we measure the transmission amplitude S_{21} of a coherent tone as a function of the detuning between the emitter qubit frequencies, $\Delta = \omega_2 - \omega_1$, and the detuning between the probe and Q_1 frequencies, $\delta = \omega_p - \omega_1$, as shown in Fig. 2a. When the qubits are detuned ($\Delta > \gamma$), they will each act as a mirror to single photons at their respective frequencies [24, 25, 30], such that there are two dips in $|S_{21}(\delta)|$. This is a consequence of the destructive interference between the probe and the forward-propagating, out-of-phase emission of the driven qubit. Therefore, $|S_{21}|$ is suppressed for weak coherent inputs (average photon number $\ll 1$) that are resonant with either qubit.

The elastic scattering behavior changes when the emitter qubits are resonant ($\Delta = 0$). First, given that the qubits are equally coupled to the waveguide, the input probe tone will only drive the $|gg\rangle \leftrightarrow |\psi(\phi)\rangle$ and $|\psi(\phi)\rangle \leftrightarrow |ee\rangle$ transitions, where $|\psi(\phi)\rangle = (|eg\rangle + e^{i\phi}|ge\rangle)/\sqrt{2}$. The sign of $\phi = \pm k\Delta x$ is determined by the propagation direction of the probe. Furthermore, the second transition can be ignored for low probe powers P , as it requires an appreciable population in $|\psi(\phi)\rangle$ to play a role. Therefore, if $\Delta x = \lambda/4$ and $\hat{H}_c = 0$, the state of the qubits will be driven into a mixture of only $|gg\rangle$ and one of $|\psi^+\rangle$ or $|\psi^-\rangle$, depending on the direction of the probe. However, these states can only re-emit photons in the same direction as the input, as depicted in the level-diagram in Fig. 2b for a rightward-propagating probe. This results in perfect transmission, $|S_{21}(\Delta = 0)| = 1$.

The magnitude of the transmission will deviate from unity if $\hat{H}_c \neq 0$, as any population transfer between $|\psi^+\rangle \leftrightarrow |\psi^-\rangle$ will cause part of the qubit emission to propagate in the direction opposite to that of the probe. To verify this, we measure $|S_{21}(\Delta = 0)|$ as a function of $|J_\Sigma|$ in Fig. 2b. For $|J_\Sigma| > \gamma/2$ we see two dips in the transmission at $\delta = \pm J_\Sigma$, which now correspond to the hybridized energy splitting of $|\psi^+\rangle$ and $|\psi^-\rangle$. For $|J_\Sigma| < \gamma/2$, the energy splitting is within the linewidth of the qubits, which is set by γ . However, as described above, we observe the $|S_{21}(\delta)| \rightarrow 1$ as $J_\Sigma \rightarrow 0$. Therefore, we can use the transmission as a metric to set $J_\Sigma = 0$ despite the large decay rate γ of these qubits.

Finally, in Fig. 2c we show the transmission $|S_{21}(\Delta = 0, \delta = 0, J_\Sigma = 0)|$ as a function of the probe power. Here, we clearly see $|S_{21}| \approx 1$ for both low powers, as previously discussed, and high powers, where the average photon number of the probe is much greater than one and the emitter qubits are fully saturated. For intermediate powers, however, the transmission is no longer unity, because the qubits are neither fully saturated nor restricted to the zero- and single-excitation subspace. That is, the population of $|ee\rangle$ and its subsequent decay into both $|\psi^\pm\rangle$ cannot be ignored, in contrast to the simpler low-power case. We numerically simulate the power-dependence of the transmission amplitude using input-output theory. The resulting simulation fits very well to the data in Fig. 2c, demonstrating the validity of our model.

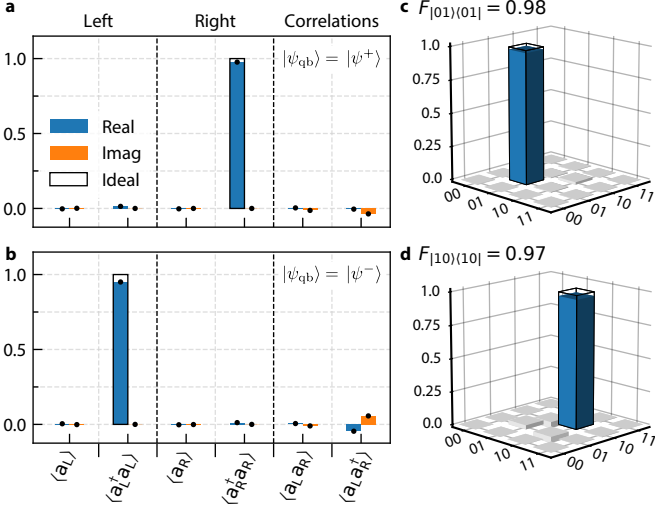


FIG. 4. Photon state tomography. **a)** The moments and correlations of the left and right propagating channels of the waveguide with $|\psi_{qb}\rangle = |\psi^+\rangle$. All moments are nearly zero, except $\langle \hat{a}_R^\dagger \hat{a}_R \rangle \approx 0.97$. **b)** The same as (a) but with $|\psi_{qb}\rangle = |\psi^-\rangle$. All moments are once again nearly zero, except $\langle \hat{a}_L^\dagger \hat{a}_L \rangle \approx 0.95$. **c)** The real part of the density matrix of the photon emitted to the right based on the moments shown in (a) with a state fidelity of $F_{|01\rangle\langle01|} = 0.98$. **d)** The real part of the density matrix of the photon emitted to the left based on the moments shown in (b) with a state fidelity of $F_{|10\rangle\langle10|} = 0.97$.

C. Photon Generation and Measurement

Having realized the conditions required to observe directional photon emission, we now run the full protocol using the pulse sequence shown in Fig. 3a. Rather than directly preparing the initial state of the emitter qubits into $|\psi^\pm\rangle$, which have low coherence due to their continuous dissipation into the waveguide, we instead initialize qubits Q_3 and Q_4 , which have longer lifetimes. We do so by first exciting either Q_3 or Q_4 while they are decoupled. Next, the frequency of the tunable coupler C_{34} is modulated at the detuning of this qubit pair to implement an entangling $\sqrt{i}\text{SWAP}$ gate [47]. Depending on which qubit was initially excited, the $\sqrt{i}\text{SWAP}$ gate will take the combined state of Q_3 and Q_4 to one of $|\psi^\pm\rangle$. Parametric exchange interactions mediated by the tunable couplers C_{13} and C_{24} are used to transfer the state of Q_3 and Q_4 into Q_1 and Q_2 (see Supplementary Info. for details), which simultaneously emit their excitations as photons. The interference process shown in Fig. 1 remains the same, but the shape of the emitted photon is now determined by both the parametrically induced coupling g_{eff} between the qubit pairs $Q_{1/2} \leftrightarrow Q_{3/4}$ and γ .

We first measure the temporal dynamics of the averaged field amplitudes $\hat{a}_{L/R}(t)$. The field amplitudes are only non-zero when there is finite coherence between the

$|00\rangle$ and $|01\rangle$ or $|10\rangle$ states. Indeed, if Q_3 and Q_4 are initialized in the state $|\psi^\pm\rangle$, such that the emitted photon is in a Fock state, the field amplitude will be zero. Therefore, we initially excite Q_3 (Q_4) with a $\frac{\pi}{2}$ -pulse, such that the emitted photon will be in the state $[|00\rangle + |01\rangle]/\sqrt{2}$ ($[|00\rangle + |10\rangle]/\sqrt{2}$). The photon wavepacket is now visible in the amplitude of the field, as shown in Figs. 3b and 3c. The amplitude of the photon is non-zero in only a single direction that is determined by the phase in the initial state of Q_3 and Q_4 , a signature of the controlled directional emission. We fit this data (see Supplementary Info.) to obtain the effective coupling between the data and emitter qubit pairs $g_{\text{eff}}/2\pi = 1.28$ MHz.

Next, we perform photon state tomography [43, 48–50] to fully reconstruct the state of the emitted photon and quantify its fidelity. We use quadrature amplitude detection of the left and right outputs of the waveguide to obtain the higher-order moments and correlations of the fields. Time-independent values of the field quadratures $S_{L/R} = X_{L/R} + iP_{L/R}$ are obtained by digitally demodulating and integrating individual records of the measured time-dependent field amplitudes. Using repeated measurements of these values, we construct a 4D probability distribution $D(S_L, S_L^*, S_R, S_R^*)$ that is used to obtain the moments of S_L and S_R ,

$$\langle \hat{S}_L^{\dagger w} \hat{S}_L^x \hat{S}_R^{\dagger y} \hat{S}_R^z \rangle = \int d^2 S_L d^2 S_R S_L^{*w} S_L^x S_R^{*y} S_R^z D(S_L, S_L^*, S_R, S_R^*), \quad (4)$$

where $w, x, y, z \in \{0, 1, 2, \dots\}$. The measured signals $S_{L/R}$ are composed of both the field of interest $\hat{a}_{L/R}$ as well as noise added by the amplification chain. This additional noise is subtracted from the moments of $\hat{S}_{L/R}$, using the input-output relations for phase-insensitive amplifiers [51], to obtain the desired moments of $\hat{a}_{L/R}$ [43, 48, 49].

The moments of and correlations between \hat{a}_L and \hat{a}_R for the photons we generate are shown in Fig. 4a and 4b. When Q_3 and Q_4 are initialized to $|\psi^+\rangle$, we obtain $\langle \hat{a}_R^\dagger \hat{a}_R \rangle \approx 1$ as the only appreciably non-zero moment, as expected for a single photon which only propagates towards the right. Similarly, we measure $\langle \hat{a}_L^\dagger \hat{a}_L \rangle \approx 1$ as the only non-zero moment for the leftward-propagating photon emitted when the qubits are initialized to $|\psi^-\rangle$. Finally, we use these moments to obtain the density matrices of the emitted photons, shown in Figs. 4c and 4d, using maximum likelihood estimation. From these density matrices, we obtain a state fidelity of $F = 0.98$ and $F = 0.97$ for the rightward- and leftward-propagating photons, respectively. We observe a small, non-zero number of photons in the right (left) output of the waveguide when the qubits are initialized to $|\psi^+\rangle$ ($|\psi^-\rangle$). This infidelity is the result of imperfect interference between the emission pathways caused by qubit decoherence during the emission and small deviations from necessary conditions $\Delta x = \lambda/4$ and $J_\Sigma = 0$.

III. DISCUSSION

Our results demonstrate that quantum interference between emitters in a waveguide QED architecture can be used to realize a directional single photon source. While we have only performed photon generation in this work, the time-reverse of the emission protocol can be used to capture photons with this same architecture if the wavepacket of the incoming photon is symmetric in time [19, 22]. Note that the wavepacket of the generated photon can be shaped arbitrarily, in principle, by varying the time-dependence of the coupling between the data and emitter qubits [19, 22, 38, 52]. Looking forward, we envision building a quantum network by tiling devices with the presented architecture in series and applying our protocol for both photon generation and capture. Such a network will enable entanglement distribution and information shuttling with high fidelity in support of extensible quantum information processing.

ACKNOWLEDGMENTS

The authors gratefully acknowledge Daniel Campbell for his contributions to the infrastructures used in this experiment, and David K. Kim for assisting with device fabrication. This research was funded in part by the

AWS Center for Quantum Computing, U.S. Army Research Office Grant No. W911NF-18-1-0411, the DOE Office of Science National Quantum Information Science Research Centers, Co-design Center for Quantum Advantage (C2QA) under Contract No. DE-SC0012704, and the Department of Defense under Air Force Contract No. FA8702-15-D-0001. B.K. gratefully acknowledges support from the National Defense Science and Engineering Graduate Fellowship program. A.A. gratefully acknowledges support from the P.D. Soros Fellowship program. Any opinions, findings, conclusions or recommendations expressed in this material are those of the author(s) and should not be interpreted as necessarily representing the official policies or endorsements of the U.S. Government.

AUTHOR CONTRIBUTIONS

B.K. designed the experiment procedure. B.K. and A.A. designed the devices, conducted the measurements, analyzed the data, and wrote the manuscript. A.D.P. provided theory support. A.M. and B.M.N. performed sample fabrication. Y.S., D.A.R., K.S., and J.I-J.W. assisted with the experimental setup. R.W. developed the custom FPGA code used to obtain the data. J.B., A.K., and A.V. assisted with the automation of the device calibration. M.E.S., J.L.Y., T.P.O., S.G., J.A.G., and W.D.O. supervised the project. All authors discussed the results and commented on the manuscript.

-
- [1] H. J. Kimble, *Nature* **453**, 1023 (2008).
- [2] J. I. Cirac, A. K. Ekert, S. F. Huelga, and C. Macchiavello, *Phys. Rev. A* **59**, 4249 (1999).
- [3] C. Monroe, R. Raussendorf, A. Ruthven, K. R. Brown, P. Maunz, L.-M. Duan, and J. Kim, *Phys. Rev. A* **89**, 022317 (2014).
- [4] I. Söllner, S. Mahmoodian, S. L. Hansen, L. Midolo, A. Javadi, G. Kirsanské, T. Pagnolato, H. El-Ella, E. H. Lee, J. D. Song, S. Stobbe, and P. Lodahl, *Nature Nanotechnology* **10**, 775 (2015).
- [5] R. J. Coles, D. M. Price, J. E. Dixon, B. Royall, E. Clarke, P. Kok, M. S. Skolnick, A. M. Fox, and M. N. Makhonin, *Nature Communications* **7**, 11183 (2016).
- [6] J. Petersen, J. Volz, and A. Rauschenbeutel, *Science* **346**, 67 (2014).
- [7] R. Mitsch, C. Sayrin, B. Albrecht, P. Schneeweiss, and A. Rauschenbeutel, *Nature Communications* **5**, 5713 (2014).
- [8] P. Lodahl, S. Mahmoodian, S. Stobbe, A. Rauschenbeutel, P. Schneeweiss, J. Volz, H. Pichler, and P. Zoller, *Nature* **541**, 473 (2017).
- [9] P. Solano, J. A. Grover, J. E. Hoffman, S. Ravets, F. K. Fatemi, L. A. Orozco, and S. L. Rolston, in *Advances In Atomic, Molecular, and Optical Physics*, Vol. 66 (Academic Press, 2017) pp. 439–505.
- [10] Y. Wan, D. Kienzler, S. D. Erickson, K. H. Mayer, T. R. Tan, J. J. Wu, H. M. Vasconcelos, S. Glancy, E. Knill, D. J. Wineland, A. C. Wilson, and D. Leibfried, *Science* **364**, 875 (2019).
- [11] J. M. Pino, J. M. Dreiling, C. Figgatt, J. P. Gaebler, S. A. Moses, M. S. Allman, C. H. Baldwin, M. Foss-Feig, D. Hayes, K. Mayer, C. Ryan-Anderson, and B. Neyenhuis, *Nature* **592**, 209 (2021).
- [12] D. Bluvstein, H. Levine, G. Semeghini, T. T. Wang, S. Ebadi, M. Kalinowski, A. Keesling, N. Maskara, H. Pichler, M. Greiner, V. Vuletic, and M. D. Lukin, “A quantum processor based on coherent transport of entangled atom arrays,” (2021), arXiv:2112.03923 [quant-ph].
- [13] Y. P. Zhong, H.-S. Chang, K. J. Satzinger, M.-H. Chou, A. Bienfait, C. R. Conner, É. Dumur, J. Grebel, G. A. Peairs, R. G. Povey, D. I. Schuster, and A. N. Cleland, *Nature Physics* **15**, 741 (2019).
- [14] N. Leung, Y. Lu, S. Chakram, R. K. Naik, N. Earnest, R. Ma, K. Jacobs, A. N. Cleland, and D. I. Schuster, *npj Quantum Information* **5**, 18 (2019).
- [15] H.-S. Chang, Y. P. Zhong, A. Bienfait, M.-H. Chou, C. R. Conner, E. Dumur, J. Grebel, G. A. Peairs, R. G. Povey, K. J. Satzinger, and A. N. Cleland, *Phys. Rev. Lett.* **124**, 240502 (2020).
- [16] Y. Zhong, H.-S. Chang, A. Bienfait, É. Dumur, M.-H. Chou, C. R. Conner, J. Grebel, R. G. Povey, H. Yan, D. I. Schuster, and A. N. Cleland, *Nature* **590**, 571 (2021).
- [17] L. D. Burkhardt, J. D. Teoh, Y. Zhang, C. J. Axline, L. Frunzio, M. Devoret, L. Jiang, S. Girvin, and R. Schoelkopf, *PRX Quantum* **2**, 030321 (2021).

- [18] J. Ramette, J. Sinclair, Z. Vendeiro, A. Rudelis, M. Cetina, and V. Vuletić, “Any-to-any connected cavity-mediated architecture for quantum computing with trapped ions or rydberg arrays,” (2021), [arXiv:2109.11551 \[quant-ph\]](https://arxiv.org/abs/2109.11551).
- [19] P. Kurpiers, P. Magnard, T. Walter, B. Royer, M. Pechal, J. Heinsoo, Y. Salathé, A. Akin, S. Storz, J.-C. Besse, S. Gasparinetti, A. Blais, and A. Wallraff, *Nature* **558**, 264 (2018).
- [20] P. Kurpiers, M. Pechal, B. Royer, P. Magnard, T. Walter, J. Heinsoo, Y. Salathé, A. Akin, S. Storz, J.-C. Besse, S. Gasparinetti, A. Blais, and A. Wallraff, *Phys. Rev. Applied* **12**, 044067 (2019).
- [21] P. Magnard, S. Storz, P. Kurpiers, J. Schär, F. Marxer, J. Lütolf, T. Walter, J.-C. Besse, M. Gabureac, K. Reuer, A. Akin, B. Royer, A. Blais, and A. Wallraff, *Phys. Rev. Lett.* **125**, 260502 (2020).
- [22] N. Gheeraert, S. Kono, and Y. Nakamura, *Phys. Rev. A* **102**, 053720 (2020).
- [23] K. Lalumi  re, B. C. Sanders, A. F. van Loo, A. Fedorov, A. Wallraff, and A. Blais, *Phys. Rev. A* **88**, 043806 (2013).
- [24] O. Astafiev, A. M. Zagorskin, A. A. Abdumalikov, Y. A. Pashkin, T. Yamamoto, K. Inomata, Y. Nakamura, and J. S. Tsai, *Science* **327**, 840 (2010).
- [25] I.-C. Hoi, C. M. Wilson, G. Johansson, T. Palomaki, B. Peropadre, and P. Delsing, *Phys. Rev. Lett.* **107**, 073601 (2011).
- [26] I.-C. Hoi, C. M. Wilson, G. Johansson, J. Lindkvist, B. Peropadre, T. Palomaki, and P. Delsing, *New Journal of Physics* **15**, 025011 (2013).
- [27] I.-C. Hoi, A. F. Kockum, L. Tornberg, A. Pourkabirian, G. Johansson, P. Delsing, and C. M. Wilson, *Nature Physics* **11**, 1045 (2015).
- [28] R. H. Dicke, *Phys. Rev.* **93**, 99 (1954).
- [29] A. F. van Loo, A. Fedorov, K. Lalumi  re, B. C. Sanders, A. Blais, and A. Wallraff, *Science* **342**, 1494 (2013).
- [30] M. Mirhosseini, E. Kim, X. Zhang, A. Sipahigil, P. B. Dieterle, A. J. Keller, A. Asenjo-Garcia, D. E. Chang, and O. Painter, *Nature* **569**, 692 (2019).
- [31] A. Frisk Kockum, P. Delsing, and G. Johansson, *Phys. Rev. A* **90**, 013837 (2014).
- [32] A. F. Kockum, G. Johansson, and F. Nori, *Phys. Rev. Lett.* **120**, 140404 (2018).
- [33] A. Frisk Kockum, in *International Symposium on Mathematics, Quantum Theory, and Cryptography*, edited by T. Takagi, M. Wakayama, K. Tanaka, N. Kunihiro, K. Kimoto, and Y. Ikematsu (Springer Singapore, Singapore, 2021) pp. 125–146.
- [34] A. M. Vadiraj, A. Ask, T. G. McConkey, I. Nsanzineza, C. W. S. Chang, A. F. Kockum, and C. M. Wilson, *Phys. Rev. A* **103**, 023710 (2021).
- [35] B. Kannan, M. J. Ruckriegel, D. L. Campbell, A. Frisk Kockum, J. Braum  ller, D. K. Kim, M. Kjaergaard, P. Krantz, A. Melville, B. M. Niedzielski, A. Veps  inen, R. Winik, J. L. Yoder, F. Nori, T. P. Orlando, S. Gustavsson, and W. D. Oliver, *Nature* **583**, 775 (2020).
- [36] A. A. Abdumalikov, O. V. Astafiev, Y. A. Pashkin, Y. Nakamura, and J. S. Tsai, *Phys. Rev. Lett.* **107**, 043604 (2011).
- [37] I.-C. Hoi, T. Palomaki, J. Lindkvist, G. Johansson, P. Delsing, and C. M. Wilson, *Phys. Rev. Lett.* **108**, 263601 (2012).
- [38] P. Forn-D  az, C. W. Warren, C. W. S. Chang, A. M. Vadiraj, and C. M. Wilson, *Phys. Rev. Applied* **8**, 054015 (2017).
- [39] A. Gonz  lez-Tudela, V. Paulisch, D. E. Chang, H. J. Kimble, and J. I. Cirac, *Phys. Rev. Lett.* **115**, 163603 (2015).
- [40] W. Pfaff, C. J. Axline, L. D. Burkhardt, U. Vool, P. Reinhold, L. Frunzio, L. Jiang, M. H. Devoret, and R. J. Schoelkopf, *Nature Physics* **13**, 882 (2017).
- [41] S. Gasparinetti, M. Pechal, J.-C. Besse, M. Mondal, C. Eichler, and A. Wallraff, *Phys. Rev. Lett.* **119**, 140504 (2017).
- [42] J.-C. Besse, K. Reuer, M. C. Collodo, A. Wulff, L. Wernli, A. Copetudo, D. Malz, P. Magnard, A. Akin, M. Gabureac, G. J. Norris, J. I. Cirac, A. Wallraff, and C. Eichler, *Nature Communications* **11**, 4877 (2020).
- [43] B. Kannan, D. L. Campbell, F. Vasconcelos, R. Winik, D. K. Kim, M. Kjaergaard, P. Krantz, A. Melville, B. M. Niedzielski, J. L. Yoder, T. P. Orlando, S. Gustavsson, and W. D. Oliver, *Science Advances* **6**, eabb8780 (2020).
- [44] J. Koch, T. M. Yu, J. Gambetta, A. A. Houck, D. I. Schuster, J. Majer, A. Blais, M. H. Devoret, S. M. Girvin, and R. J. Schoelkopf, *Phys. Rev. A* **76**, 042319 (2007).
- [45] F. Yan, P. Krantz, Y. Sung, M. Kjaergaard, D. L. Campbell, T. P. Orlando, S. Gustavsson, and W. D. Oliver, *Phys. Rev. Applied* **10**, 054062 (2018).
- [46] Y. Sung, L. Ding, J. Braum  ller, A. Veps  inen, B. Kannan, M. Kjaergaard, A. Greene, G. O. Samach, C. McNally, D. Kim, A. Melville, B. M. Niedzielski, M. E. Schwartz, J. L. Yoder, T. P. Orlando, S. Gustavsson, and W. D. Oliver, *Phys. Rev. X* **11**, 021058 (2021).
- [47] D. C. McKay, S. Filipp, A. Mezzacapo, E. Magesan, J. M. Chow, and J. M. Gambetta, *Phys. Rev. Applied* **6**, 064007 (2016).
- [48] C. Eichler, D. Bozyigit, C. Lang, L. Steffen, J. Fink, and A. Wallraff, *Phys. Rev. Lett.* **106**, 220503 (2011).
- [49] C. Eichler, D. Bozyigit, and A. Wallraff, *Phys. Rev. A* **86**, 032106 (2012).
- [50] C. Lang, C. Eichler, L. Steffen, J. M. Fink, M. J. Woolley, A. Blais, and A. Wallraff, *Nature Physics* **9**, 345 (2013).
- [51] C. M. Caves, *Phys. Rev. D* **26**, 1817 (1982).
- [52] K. Reuer, J.-C. Besse, L. Wernli, P. Magnard, P. Kurpiers, G. J. Norris, A. Wallraff, and C. Eichler, *Phys. Rev. X* **12**, 011008 (2022).
- [53] T. F. Havel, *Journal of Mathematical Physics* **44**, 534 (2003).

SUPPLEMENTARY INFORMATION

Device and Experimental Setup

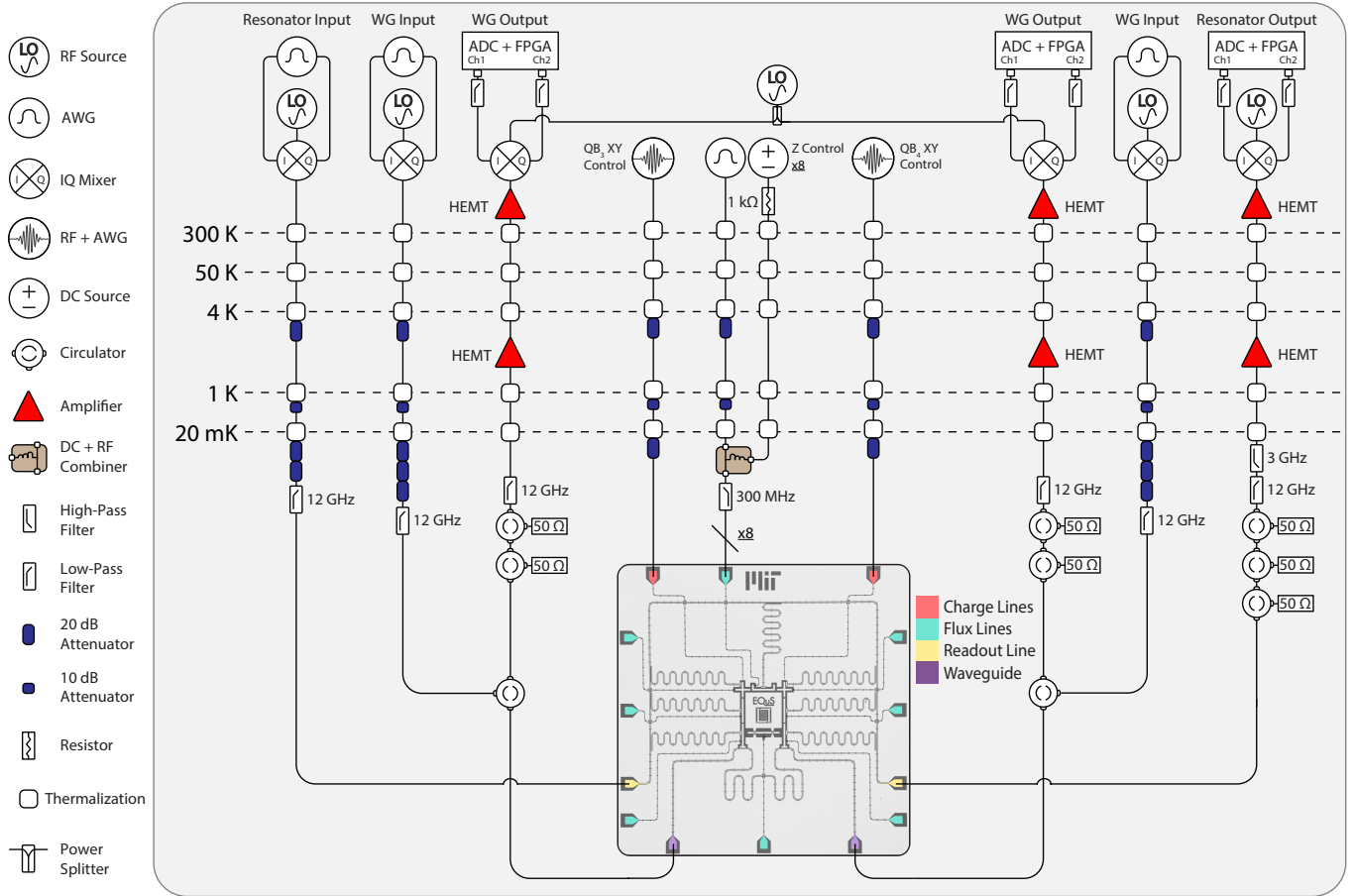


FIG. S1. Experimental setup. Wiring schematic of the device and all electronics used to perform the experiment. Note that only one flux line configuration is shown (green), but each qubit and coupler is coupled to a flux line with separate, but identical, control electronics.

This experiment was conducted in a Bluefors XLD1000 dilution refrigerator, which can reach a base temperature of 10 mK. The experimental setup is shown in Fig. S1. The device is protected from ambient magnetic fields by superconducting and Cryoperm-10 shields below the mixing chamber (MXC). Each end of the waveguide is connected to a microwave circulator for dual input-output operation. To minimize thermal noise from higher temperature stages, the inputs are attenuated by 20 dB at the 4K stage, 10 dB at the 1K stage, and 60 dB (40 dB for resonator readout input) at the MXC. The output signals are filtered with 3 GHz high-pass and 12 GHz low-pass filters. Two additional isolators are placed after the circulator in the MXC to prevent noise from higher-temperature stages travelling back into the sample. High electron mobility transistor (HEMT) amplifiers are used at 4 K and room-temperature stages of the measurement chain to amplify the outputs from the device. The signals are then downconverted to an intermediate frequency using an IQ mixer, filtered, digitized, and demodulated. All qubits and tunable couplers are also equipped with their own flux bias lines. A DC + RF combiner is used for all flux lines to provide both static and dynamic control of the qubit/coupler frequencies. The DC and RF inputs are joined by a RF choke below the MXC before passing through a 300 MHz low pass filter. The RF flux control lines are attenuated by 20 dB at the 4K stage, and by 10 dB at the 1K stage. The data qubits are equipped with local charge lines for independent single-qubit XY gates. The specific control and measurement equipment used throughout the experiment is summarized in Table S1. The relevant parameters of the device used in the experiment are summarized in Table S2.

| Component | Manufacturer | Model |
|-----------------|-----------------|---------|
| Dilution Fridge | Bluefors | XLD1000 |
| RF Source | Rohde & Schwarz | SGS100 |
| DC Source | QDevil | QDAC |
| Control Chassis | Keysight | M9019A |
| AWG | Keysight | M3202A |
| ADC | Keysight | M3102A |

TABLE S1. **Summary of control equipment.** The manufacturers and model numbers of the control equipment used for the experiment.

| Parameter | Q ₁ | Q ₂ | Q ₃ | Q ₄ |
|--------------------|----------------|----------------|----------------|----------------|
| Frequency | 4.93 GHz | 4.93 GHz | 4.8 GHz | 4.85 GHz |
| Anharmonicity | -274 MHz | -273 MHz | -307 MHz | -307 MHz |
| $\gamma/2\pi$ | 3.2 MHz | 3.2 MHz | - | - |
| $\gamma_\phi/2\pi$ | 8 kHz | 42 kHz | - | - |
| T_1 | - | - | 13.8 μ s | 13.4 μ s |
| T_2^* | - | - | 18.1 μ s | 23.6 μ s |

TABLE S2. **Summary of device parameters.** The operational qubit frequencies, anharmonicities, emitter-waveguide coupling strengths γ , emitter dephasing rates γ_ϕ , and T_1 and T_2^* of the data qubits are given for the emitter (Q_{1/2}) and data qubits (Q_{3/4}) on the device used throughout the experiment.

Spectroscopic Measurements

We measure the elastic scattering of a coherent input into the waveguide in order to extract device parameters that involve the emitter qubits. Consider a single emitter qubit that is strongly coupled to the waveguide with strength γ . The qubit will scatter coherent probe tones sent through the waveguide in a manner such that it acts as a mirror to single photons. Therefore, the scattering parameters will strongly depend on the probe power, since this is what determines the number of photons incident upon the emitter [24–26]. The master equation for the simplified model of a single emitter coupled to a waveguide is given by [30]

$$\partial_t \hat{\rho} = -i[\hat{H}, \hat{\rho}] + \gamma D[\hat{\sigma}^-] \hat{\rho} + \frac{\gamma_\phi}{2} D[\hat{\sigma}_z]. \quad (\text{S1})$$

The single-emitter Hamiltonian is $\hat{H} = \frac{1}{2}\delta\hat{\sigma}_z + \frac{1}{2}\Omega_p\hat{\sigma}_x$, γ_ϕ is the pure dephasing rate of the emitter, $\delta = \omega - \omega_p$ is the emitter-probe detuning, and $\Omega_p = \sqrt{2\gamma P/\hbar\omega}$ is the drive strength of the probe with power P . Assuming that the probe propagates towards the right, the right-ward propagating output of the waveguide can be determined via input-output theory:

$$\hat{a}_R = \hat{a}_R^{\text{in}} + \sqrt{\frac{\gamma}{2}} \hat{\sigma}^-. \quad (\text{S2})$$

Therefore, the transmission amplitude $S_{21} = \langle \hat{a}_R \rangle / \langle \hat{a}_R^{\text{in}} \rangle$ can be calculated to be [30]

$$S_{21}(\delta, \Omega_p) = 1 - \frac{\gamma(1 - i\frac{\delta}{\gamma_2})}{2\gamma_2 \left(1 + \left(\frac{\delta}{\gamma_2} \right)^2 + \frac{\Omega_p^2}{\gamma\gamma_2} \right)}, \quad (\text{S3})$$

where $\gamma_2 = \gamma/2 + \gamma_\phi$ is the total decoherence rate of the emitter. Transmission measurements as a function of probe power P and detuning δ , as shown in Fig. S2, allow us to obtain the fit parameters such as $\gamma/2\pi \approx 3.2$ MHz and $\gamma_\phi/2\pi \approx 8$ kHz (41 kHz). These measurements serve as a method to calibrate the absolute power of microwave tones incident on the emitter qubits.

Parametric Exchange Interactions

The exchange interactions used in the main text were mediated by the parametric modulation of the tunable coupler frequencies. To see this, consider two qubits at frequencies ω_i and ω_j , and a tunable coupler at frequency ω_c , as illustrated in Fig. S3a. Each qubit is capacitively coupled to the tunable coupler at rates g_{ic} and g_{jc} , and to each

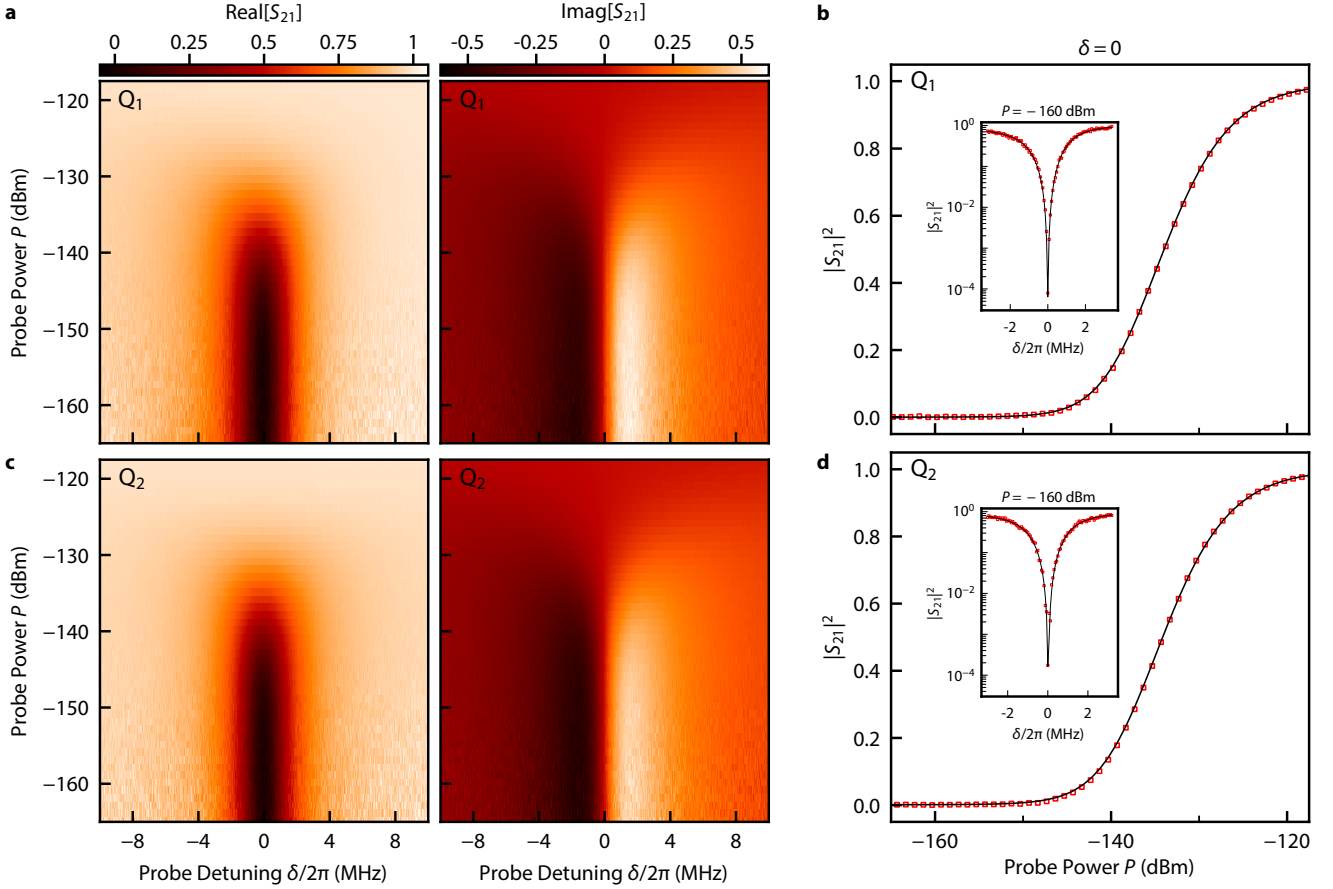


FIG. S2. Emitter qubit spectroscopy. a, c) Real (left) and imaginary (right) components of the transmission spectrum of a coherent probe incident on Q_1 (Q_2) through the waveguide as a function of the qubit-probe detuning $\delta/2\pi$ and the probe power P . We extract the qubit-waveguide coupling rate $\gamma/2\pi = 3.2$ MHz and the qubit dephasing rate $\gamma_\phi/2\pi = 8$ kHz (42 kHz). b, d) Transmittance $|S_{21}|^2$ as a function of probe power P at zero qubit-probe detuning ($\delta/2\pi = 0$). The measured data is plotted in red, and the theoretical fit is plotted in black. The inset shows the frequency response of the emitter qubit at probe power $P = -160$ dBm.

other at rate g_{ij} . The coupler is far-detuned from both qubit frequencies $\omega_c - \omega_{i,j} \gg g_{ic}, g_{jc}, g_{ij}$, and the qubits are slightly detuned by $\Delta = \omega_j - \omega_i$. The Hamiltonian of the system in the rotating frame of the qubit Q_i is [45]

$$\hat{H} = \Delta \sigma_j^+ \sigma_j^- + \left(\frac{g_{ic} g_{jc}}{\delta} + g_{ij} \right) (\sigma_i^+ \sigma_j^- + \sigma_i^- \sigma_j^+), \quad (\text{S4})$$

where $\delta = 2 \left(\frac{1}{\omega_i - \omega_c} + \frac{1}{\omega_j - \omega_c} \right)^{-1} = 2 \left(\frac{1}{\delta_i} + \frac{1}{\delta_j} \right)^{-1}$. The coupling rates g_{ic}, g_{jc} , and g_{ij} are determined by the the qubit frequencies and the capacitances C_{ij} , C_c , C_i/C_j , and $C_{j,c}/C_{i,c}$ as defined in Fig. S3a:

$$\begin{aligned} g_{ij} &\approx \frac{1}{2} \left(\frac{C_{ij}}{\sqrt{C_i C_j}} + \frac{C_{i,c} C_{j,c}}{\sqrt{C_i C_j C_c^2}} \right) \sqrt{\omega_i \omega_j} = \frac{\tilde{C}_{ij}}{2} \sqrt{\omega_i \omega_j}, \\ g_{nc} &\approx \frac{C_{n,c}}{2\sqrt{C_n C_c}} \sqrt{\omega_n \omega_c} = \frac{\tilde{C}}{2} \sqrt{\omega_n \omega_c} \quad n = i, j. \end{aligned} \quad (\text{S5})$$

Here, we assume that Q_i and Q_j are identical qubits, with equal self-capacitances $C_i = C_j$ and capacitances to the coupler $C_{i,c} = C_{j,c}$. Substituting these expressions for the coupling rates into the Hamiltonian gives

$$\hat{H} = \Delta \sigma_j^+ \sigma_j^- + \sqrt{\omega_i \omega_j} \left(\frac{\tilde{C}^2 \omega_c}{4\delta} + \frac{\tilde{C}_{ij}}{2} \right) (\sigma_i^+ \sigma_j^- + \sigma_i^- \sigma_j^+). \quad (\text{S6})$$

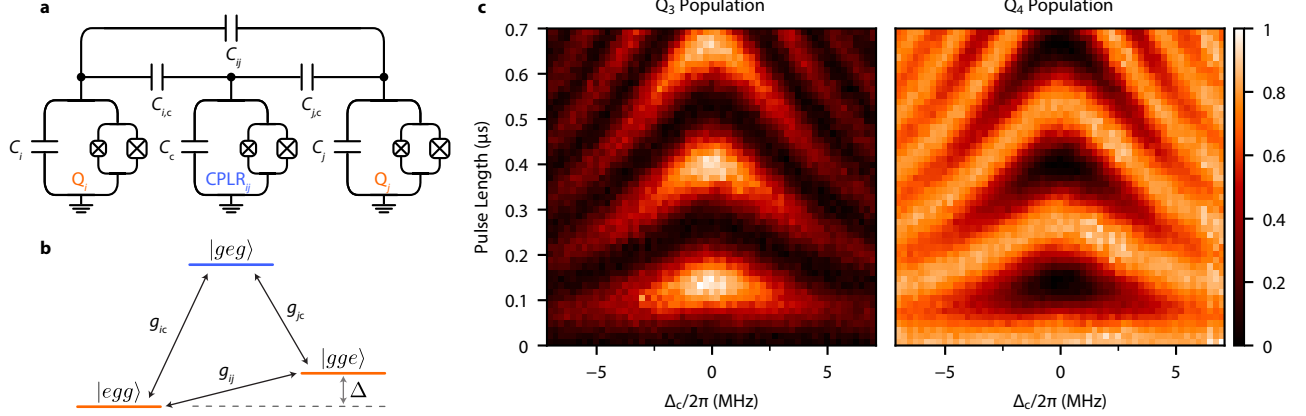


FIG. S3. Parametric interactions with a tunable coupler. a) The circuit diagram of a system with a tunable coupler CPLR_{ij} capacitively coupled two tunable transmon qubits Q_i and Q_j. The coupling capacitance between the qubits is C_{ij} and the coupling capacitances between each qubit and the coupler is C_{i,c} (C_{j,c}). b) The single-excitation manifold level diagram of the system. The coupler frequency ω_c is far-detuned from the frequencies of the qubits ω_i and ω_j, and the two qubits are slightly detuned from each other by Δ = ω_j − ω_i. The capacitance between the qubits C_{ij} mediates a direct coupling with strength g_{ij}. The capacitances between the coupler and each qubit give rise to couplings between each qubit-coupler pair at the rates g_{ic} and g_{jc}. c) The measured population exchange between qubits Q₃ and Q₄ as a function of the parametric modulation pulse length and frequency offset Δ_c = δ_c − Δ, where δ_c is the frequency of the modulation.

Next, we modulate the frequency of the tunable coupler ω_c = ω_{c0} + A cos Δt. In practice, this is realized by modulating the flux applied into the SQUID loop of the coupler. Since ω_c ≫ ω_i, ω_j, we can approximate the total detuning as δ ≈ δ_i = ω_i − ω_c. Assuming the amplitude of the coupler frequency modulation A ≪ δ_i, we separate the qubit coupling into a static component and a time-varying component,

$$\hat{H} = \Delta\sigma_j^+\sigma_j^- + \sqrt{\omega_i\omega_j} \left(\frac{\tilde{C}^2\omega_{c0}}{4\delta} + \frac{\tilde{C}_{ij}}{2} + \frac{\tilde{C}^2A \cos \Delta t}{4\delta} \right) (\sigma_i^+\sigma_j^- + \sigma_i^-\sigma_j^+). \quad (\text{S7})$$

Finally, we rotate into the frame of the qubit detuning Δ and neglect the fast rotating terms. This approximation holds as long as the effective coupling rate g_{eff} ≪ Δ. The final time-independent Hamiltonian is given by

$$\hat{H} = \frac{A\tilde{C}^2\sqrt{\omega_i\omega_j}}{8\delta} (\sigma_i^+\sigma_j^- + \sigma_i^-\sigma_j^+). \quad (\text{S8})$$

This Hamiltonian shows that the two detuned qubits Q_i and Q_j are effectively coupled at rate g_{eff} = A3 and Q₄ mediated by a parametric exchange interaction. Note that we can also vary the effective coupling rate as a function of time by varying the frequency modulation amplitude A(t). This feature can be used to shape the wavepacket of the emitted photon, which will be necessary in future work for perfect absorption of the emitted photons [19, 22, 38, 52].

Time-Domain Measurements

In Fig. 3b/c of the main text, we showed the temporal dynamics of the photon wavepacket. Here, we analytically derive the shape of the wavepacket. We prepared the data qubits in the state |ψ_{qb}[±]⟩ = (|gg⟩ + |ψ[±]⟩)/√2. The state of the data qubits was then transferred to the emitter qubits with parametric exchange interactions as part of the photon release protocol. The four-qubit master equation that describes this system is written as

$$\partial_t \hat{\rho} = -i[\hat{H}, \hat{\rho}] + \sum_{k=1,2} \hat{c}_k \hat{\rho} \hat{c}_k^\dagger - \frac{1}{2} \{ \hat{c}_k^\dagger \hat{c}_k, \hat{\rho} \}, \quad (\text{S9})$$

where

$$\hat{H} = g_{\text{eff}} (\hat{\sigma}_3^- \hat{\sigma}_1^+ + \hat{\sigma}_3^+ \hat{\sigma}_1^-) + g_{\text{eff}} (\hat{\sigma}_4^- \hat{\sigma}_2^+ + \hat{\sigma}_4^+ \hat{\sigma}_2^-), \quad (\text{S10})$$

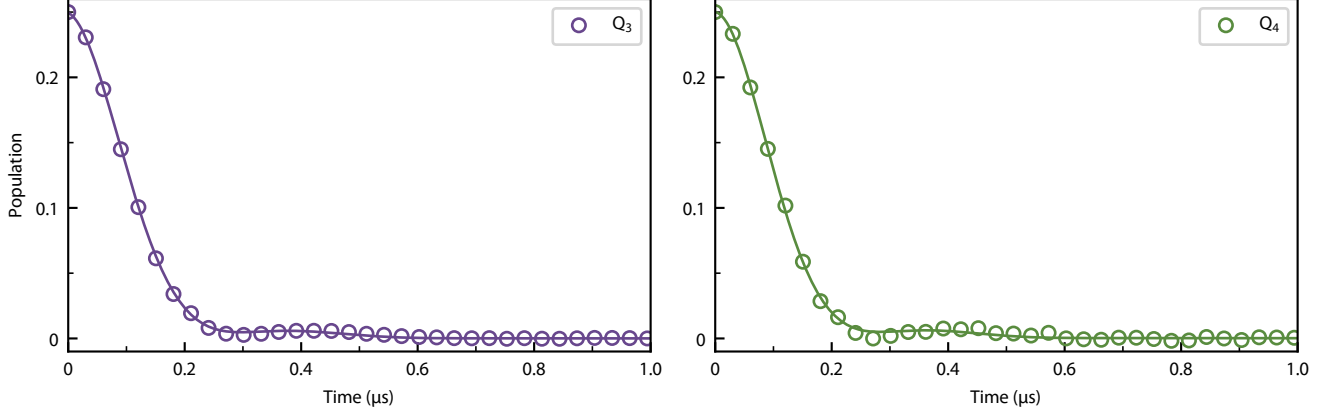


FIG. S4. Excited state population of data qubits during photon emission. We utilize dispersive readout to measure the population of the data qubits during the photon release protocol immediately after the initialization of the data qubits into the state $|\psi_{\text{qb}}^{\pm}\rangle = |gg\rangle/\sqrt{2} + (|eg\rangle + e^{\pm i\frac{\pi}{2}}|ge\rangle)/2$. The theoretical fit of the population is presented as a solid line in both plots.

is the system's Hamiltonian and

$$\hat{c}_k \in \{\sqrt{\gamma}\hat{\sigma}_1^-, \sqrt{\gamma}\hat{\sigma}_2^-\}, \quad (\text{S11})$$

are the collapse operators. The raising and lowering operators of each qubit Q_i is denoted as $\hat{\sigma}_i^{\pm}$, where $i \in \{1, 2, 3, 4\}$ is the qubit number as defined in the main text.

We work in the superoperator representation of Eq. S9. Vectorizing the density matrix as $\hat{\rho} \rightarrow |\rho\rangle\rangle$, we rewrite the master equation as

$$\partial_t |\rho\rangle\rangle = \hat{\mathcal{L}} |\rho\rangle\rangle, \quad (\text{S12})$$

where $\hat{\mathcal{L}}$ is the Liouvillian superoperator [53]

$$\hat{\mathcal{L}} = -i \left(\mathbb{1} \otimes \hat{H} - \hat{H}^T \otimes \mathbb{1} \right) + \sum_k \hat{c}_k^* \otimes \hat{c}_k - \frac{1}{2} \left(\mathbb{1} \otimes \hat{c}_k^\dagger \hat{c}_k + \hat{c}_k^T \hat{c}_k^* \otimes \mathbb{1} \right) \quad (\text{S13})$$

We can formally express the solution to Eq. S12 as

$$|\rho(t)\rangle\rangle = \hat{S}(t)|\rho(0)\rangle\rangle, \quad (\text{S14})$$

where $\hat{S}(t) = \exp(\hat{\mathcal{L}} t)$ is the quantum channel described by the original master equation in superoperator form. In this simplified model, the subspace formed by Q_1 and Q_3 is not coupled to the subspace formed by Q_2 and Q_4 , which allows us to write the Liouvillian superoperator as $\hat{\mathcal{L}} = \hat{\mathcal{L}}_{13} + \hat{\mathcal{L}}_{24}$, where $\hat{\mathcal{L}}_{13(24)}$ is the Liouvillian superoperator of each two-qubit subsystem. Because $\hat{\mathcal{L}}_{13}$ and $\hat{\mathcal{L}}_{24}$ commute, we can factorize the quantum channel as

$$\hat{S}(t) = \exp(\hat{\mathcal{L}}_{13} t) \cdot \exp(\hat{\mathcal{L}}_{24} t). \quad (\text{S15})$$

We solve for the density matrix of the four-qubit system $\hat{\rho}$, which we use to compute system observables, i.e. $\langle \hat{O} \rangle = \text{Tr}[\hat{\rho} \hat{O}]$. First, we examine the data qubit population as a function of time during the photon release. We obtain the analytical expression for the excited state population of each data qubit as a function of time:

$$\rho_{33}^{(d)}(t) = \rho_{44}^{(d)}(t) = \frac{e^{-\frac{\gamma}{2}t}}{16\Gamma^2} \left[(\gamma^2 - 8g_{\text{eff}}^2) \cosh(\Gamma t) + 2\gamma\Gamma \sinh(\Gamma t) - 8g_{\text{eff}}^2 \right], \quad (\text{S16})$$

where we define $\Gamma = 2\sqrt{\left(\frac{\gamma}{4}\right)^2 - g_{\text{eff}}^2}$. We use Eq. S16 to fit the dispersive readout measurement of the data qubits during the photon release protocol, shown in Fig. S4. The decay in population here corresponds to its transfer into the emitter qubits and subsequent release into the waveguide.

To obtain the temporal wavepacket of the emission field amplitude, we use the input-output relations:

$$\begin{aligned}\langle \hat{a}_L \rangle &= \sqrt{\frac{\gamma}{2}} (\langle \hat{\sigma}_1^- \rangle + \langle \hat{\sigma}_2^- \rangle e^{i\frac{\pi}{2}}), \\ \langle \hat{a}_R \rangle &= \sqrt{\frac{\gamma}{2}} (\langle \hat{\sigma}_1^- \rangle + \langle \hat{\sigma}_2^- \rangle e^{-i\frac{\pi}{2}}).\end{aligned}\tag{S17}$$

Here, we assume that there is no input into the waveguide $\langle \hat{a}_{L/R}^{\text{in}} \rangle = 0$. Using the solution to the master equation, we compute the wavepacket shape, given the initial state of the emitter qubits:

$$\begin{aligned}|\psi_{qb}^-\rangle &= \frac{|gg\rangle + |\psi^-\rangle}{\sqrt{2}} \quad \rightarrow \quad \langle \hat{a}_L \rangle = -\frac{g_{\text{eff}}\sqrt{\gamma}}{\Gamma} e^{-\frac{\gamma}{4}t} \sinh\left(\frac{\Gamma}{2}t\right), \quad \langle \hat{a}_R \rangle = 0, \\ |\psi_{qb}^+\rangle &= \frac{|gg\rangle + |\psi^+\rangle}{\sqrt{2}} \quad \rightarrow \quad \langle \hat{a}_R \rangle = \frac{g_{\text{eff}}\sqrt{\gamma}}{\Gamma} e^{-\frac{\gamma}{4}t} \sinh\left(\frac{\Gamma}{2}t\right), \quad \langle \hat{a}_L \rangle = 0,\end{aligned}\tag{S18}$$

which is used to fit the photon field amplitudes in Fig. 3b/c and extract the effective coupling between each emitter/data qubit pair $g_{\text{eff}}/2\pi \approx 1.28$ MHz.